



Design and evaluation of Cu-modified ZnO microspheres as a high performance formaldehyde sensor based on density functional theory



Yan Chen^a, Yong Zhang^b, Hongyan Zhang^{a,*}, Chu Chen^{a,*}

^a School of Physical Science and Technology, Xinjiang University, Urumqi 830046, PR China

^b Department of Physics and Optical Science, The University of North Carolina at Charlotte, NC 28223, USA

ARTICLE INFO

Keywords:

Gas sensor
Cu-modified ZnO
Formaldehyde detection
First-principles

ABSTRACT

Based on Cu-modified ZnO (CZO), a highly sensitive gas sensor for formaldehyde (HCHO) detection at room temperature was prepared by the sol-gel method, and the sensing mechanism was studied by density functional theory. Calculations indicate that the binding energy of CZO to HCHO is higher than that of pure ZnO when Cu metal occupies the oxygen vacancy on the surface of ZnO, which is beneficial for CZO to capture more HCHO molecules. Moreover, Cu metal splits oxygen molecules in the air to form a large number of oxygen free radicals on the surface of CZO and react with HCHO molecules. The lowest band gap can be obtained when HCHO is adsorbed in CZO compared to other gases, which means CZO has better selectivity in the detection for HCHO. Experiments show that Cu metal can effectively improve the performance of ZnO for HCHO detection. CZO with 3 mol% Cu exhibits short response/recovery times (1.7 s/2.9 s) and the limit of detection (LOD) is 0.61 ppm at HCHO concentration of 1 ppm. Moreover, CZO displays the excellent endurance to humidity. Such a metal-modified ZnO offers great potential for the development of highly sensitive gas sensor for HCHO detection.

1. Introduction

Formaldehyde (HCHO) is a colorless and irritating gas, which is widely used in construction, textile, decoration, furniture, chemical industry and printing. HCHO is also considered to be one of the most common indoor pollutants because it seriously endangers human health [1,2]. For example, HCHO can damage eyes, nose, respiratory tract and genes, and it can be easy to cause cancer at very low ppm concentrations [3–5]. In addition, HCHO has been placed on the list of carcinogens by the International Agency for Research on Cancer (IARC) and was identified as a toxic and harmful water pollutant by the World Health Organization (WHO) in 2019 [6]. Furthermore, the WHO and the (US) National Institute of Occupational Safety and Health (NIOSH) have established safety limitation standards for HCHO to be 0.08 ppm and 1 ppm, respectively [7,8]. Therefore, it is very important to develop a gas sensor with a low detection limit, fast response and good selectivity to detect HCHO in the living environment.

Metal oxides such as SnO₂ [8–10], ZnO [11–12], WO₃ [13], In₂O₃ [14–15], Co₃O₄ [16], NiO [17] and CdIn₂O₄ [18], have been widely used in various gas sensors due to easy fabrication, low power consumption and large specific surface area. Among them, as a typical n-type metal oxide semiconductor, ZnO has been widely used in the detection of a variety of gases due to its non-toxicity, good chemical

properties, thermal stability and easy size control [19–24]. However, pure ZnO sensors are limited in practical applications because of its poor linearity, low sensitivity and slow response [25]. There are many methods to improve the performances of ZnO gas sensors, such as doping, alloying and modifying [12,19,23]. Recently, it has been reported that the performance as a gas sensor can be effectively improved when ZnO is modified with metal elements. For example, Au-modified ZnO nanowires for detecting hydrogen (H₂) have been reported by O. Lupan et al. [26]; Pd modified ZnO nanosheets for detecting methane (CH₄) by Y. Wang et al. [27]; Fe modified nanostructured ZnO for detecting alcohol (C₂H₆O) by I. A. Pronin et al. [28]. In those reports, metals play a crucial role in improving sensitivity and response of ZnO gas sensors due to three facts: firstly, high catalytic activity which increases the reactivity of space charge layer; secondly, the change of surface resistance which increases surface conductivity; and thirdly, more activated oxygen molecules on the surface of the semiconductor which is benefit for capturing gas molecules. Among the metals, copper (Cu) has been used to enhance the oxygen adsorption capacity on the surface of semiconductor, thereby enhancing the solid-gas interaction [29]. However, as far as we know, there are very few reports on both HCHO sensors based on Cu modified ZnO and the operation mechanism. Therefore, it is imperative to study the HCHO gas sensor based on Cu metal-modified ZnO (CZO) and further to study its sensing

* Corresponding authors.

E-mail addresses: zhy@xju.edu.cn, zhanghyxj@163.com (H. Zhang), chenchu@xju.edu.cn (C. Chen).

<https://doi.org/10.1016/j.apsusc.2020.147446>

Received 2 February 2020; Received in revised form 14 July 2020; Accepted 2 August 2020

Available online 06 August 2020

0169-4332/ © 2020 Elsevier B.V. All rights reserved.

mechanism. There are many methods to synthesize ZnO, such as hydrothermal [11,21], wet-chemical [12], solvothermal reaction [22] and sol-gel method [30] et al. Among these methods, sol-gel method has advantages of excellent chemical uniformity and controllable microstructures, which attracts the attention of researcher [31–32].

In this work, gas-sensitive material of CZO was prepared by a sol-gel method, and the mechanism was studied by first-principles calculations. Calculations show that Cu metal splits oxygen molecules in the air to form a large number of free oxygen radicals on the surface of ZnO. The binding energy of HCHO on CZO increases when Cu occupies oxygen vacancy on the surface of ZnO, which helps CZO capture more HCHO molecules and react with oxygen molecules. Compared to other target gases, the lowest band gap was obtained when HCHO adsorbed in CZO sensor. Experiments show that CZO gas sensor for HCHO detection has higher sensitivity, lower limit detection (0.61 ppm) and shorter recovery time (1.7 s/2.9 s) than that of pure ZnO at room temperature. Moreover, CZO gas sensor displays an excellent endurance to humidity. These results indicate that the Cu-modification can effectively improve the performance of ZnO gas sensor for HCHO detection.

2. Experiments

2.1. Materials

Zinc acetate ((CH₃COO)₂Zn·2H₂O), copper chloride (CuCl₂, 98%) and ethanolamine (HOCH₂CH₂NH₂, 99.0–100.5%) were purchased from Zhiyuan (Tianjin, China, www.zhiyuanhx.cn.alibaba.com). All of those reagents can be used directly without further purification. Deionized water was used throughout the experiments. Ag-Pd interdigitated electrode sheet was purchased from Beijing Elite Technology Co., Ltd.

2.2. Synthesis of Cu-modified ZnO

Pure ZnO and Cu-modified ZnO (CZO) were prepared by sol-gel method [30].

Firstly, 2.3 g (CH₃COO)₂Zn·2H₂O and a certain amount of CuCl₂ were dissolved in a mixture of 20 mL ethanol and 10 mL deionized water to be vigorously stirred for 10 min at 60 °C. In this procedure, the molar ratios of Cu²⁺ to Zn²⁺ were 0 mol%, 1 mol%, 3 mol% and 5 mol %, respectively. Then 1 mL ethanolamine was dripped gradually into the above solution with magnetic stirring for 2 h at 65 °C to acquire uniform blue sol. The above blue sol was placed at room temperature for 36 h and then was placed in a constant temperature oven at 60 °C for 2 h. Eventually, the precipitation was annealed in a chemical vapor deposition (CVD) quartz tubular furnace in nitrogen (N₂) atmosphere at 600 °C for 2 h and ground to pure ZnO and CZO powder.

2.3. Characterization

Crystal structures of the samples were characterized by X-ray diffraction (XRD) (Bruker D8 Advance, where Cu-K_α radiation operates at 40 kV and 40 mA). Surface morphology of the samples was measured by scanning electron microscope (FE-SEM, S-4800, Japan). The TEM images were measured by a transmission electron microscope (TEM, JEM-2100F, Japan). The surface properties of the samples were recorded by Fourier transform infrared (FT-IR) spectrometer (Bruker-V Vertex 70, Karlsruhe, Germany). The absorption spectra were measured by a UV-vis spectrophotometer (PerkinElmer, Lambda 650, US). The elemental compositions were analyzed by ESCALAB 250Xi X-ray photoelectron spectrometer (Thermo Fisher Scientific, US, using Al K Alpha 1486.6 eV as excitation source). The I-V curves were measured at room temperature by CIMPS-2 electrochemical workstation (ZAHNER ENNIUM).

2.4. Preparation of gas sensing device

The prepared CZO powder and an appropriate amount of deionized water were placed in an agate mortar and ground for 10 min. A small brush was used to gently dip the mixed solution to be evenly applied on the Ag-Pd interdigitated electrode sheet and dried in an oven at 60 °C for 10 min. Then it was aged at room temperature for 48 h to ensure good stability. In this experiment, gas sensing performance was measured by electrochemical workstation (CIMPS-2, ZAHNER ENNIUM) with 1 V voltage at room temperature (25 °C).

2.5. Calculations

The electronic structure and the energy of metal oxide (ZnO) have been calculated by the first-principles based on the density functional theory (DFT). The DFT calculation is usually based on the stationary calculation (T = 0 K). All the calculations were carried out by the Dmol 3 code, using generalized gradient approximation (GGA) together with Perdew-Becke-Ernzerh (PBE) to describe the exchange-correlation interactions of electrons [33]. The PBE method was used to describe the electronic properties of ZnO (unit cell, band gap, etc.) in many studies. Anomalous pressure effects on the thermal conductivity of ZnO, GaN and AlN from first-principles calculations have been reported by K.P. Yuan et al [34], theoretical study on group III elements and F co-doped ZnO have been reported by J.N. Ma et al [35], and the double numeric quality basis were set with polarization functions (DNP). In those calculations, the type of ZnO structure is wurtzite. Space group and structure are one-dimensional nanorods corresponding to (001) plane. We first optimize ZnO structure and then insert copper atom on surface of ZnO. A ZnO supercell includes 94 atoms (48 Zn atoms and 46 O atoms). The removal of two O atoms corresponds to two oxygen vacancies, and two Cu atoms are located on the oxygen vacancy sites. Cu is the most stable state in the oxygen vacancy, and the binding energy between ZnO and Cu is also the largest. So the CZO simulated position started at the oxygen vacancy. A 1 × 1 × 11 k-mesh was employed for structural relaxation without any symmetry restriction. The spin-unrestricted self-consistent field calculation was set to converge to below 10⁻⁶ a.u.. The energy convergence is less than 10⁻⁵ a.u.. The maximum force was set to converge as 0.004 Hartree Å⁻¹ (1 Hartree = 27.2 eV), and the maximum displacement parameter was chosen to be 0.005 Å. To accelerate convergence, smearing value was set to be 0.002 Hartree. The transition state (TS) search was used to obtain energy maximum based on the complete linear synchronous transit (LST)/quadratic synchronous transit (QST) method [36]. Then the TS confirmation based on the nudged elastic band (NEB) method was used to calculate energy barriers [37] with the equation as the following:

$$E_{\text{Bar}} = E_{\text{Tra}} - E_{\text{In}} \quad (1)$$

where E_{Bar} , E_{In} and E_{Tra} are energies of potential barrier, initial state and transition state, respectively [37]. The binding energy of HCHO (ΔE_{HCHO}) is calculated by the equation:

$$\Delta E_{\text{HCHO}} = E_{\text{total}}(\text{HCHO} + 2\text{CZO}) - E_{\text{total}}(2\text{CZO}) - E_{\text{total}}(\text{HCHO}) \quad (2)$$

where E_{total} denotes the total energy of the corresponding system [38].

3. Results and discussions

3.1. Characterization of Cu-modified ZnO

XRD patterns of ZnO and CZO are shown in Fig. 1(a). All the samples exhibit diffraction peaks at 2θ of 31.72°, 34.45°, 36.31°, 47.44°, 56.60°, 62.81°, 66.37°, 67.83°, 69.07°, 72.63° and 76.94°, which correspond to (100), (002), (101), (102), (110), (200), (112), (201), (004) and (202) faces of ZnO (JCPDS No. 79-0205), respectively. Sharp peaks in all XRD patterns demonstrate that ZnO and CZO are highly crystallized. The diffraction peaks of 43.3°, 50.4° and 74.1° for

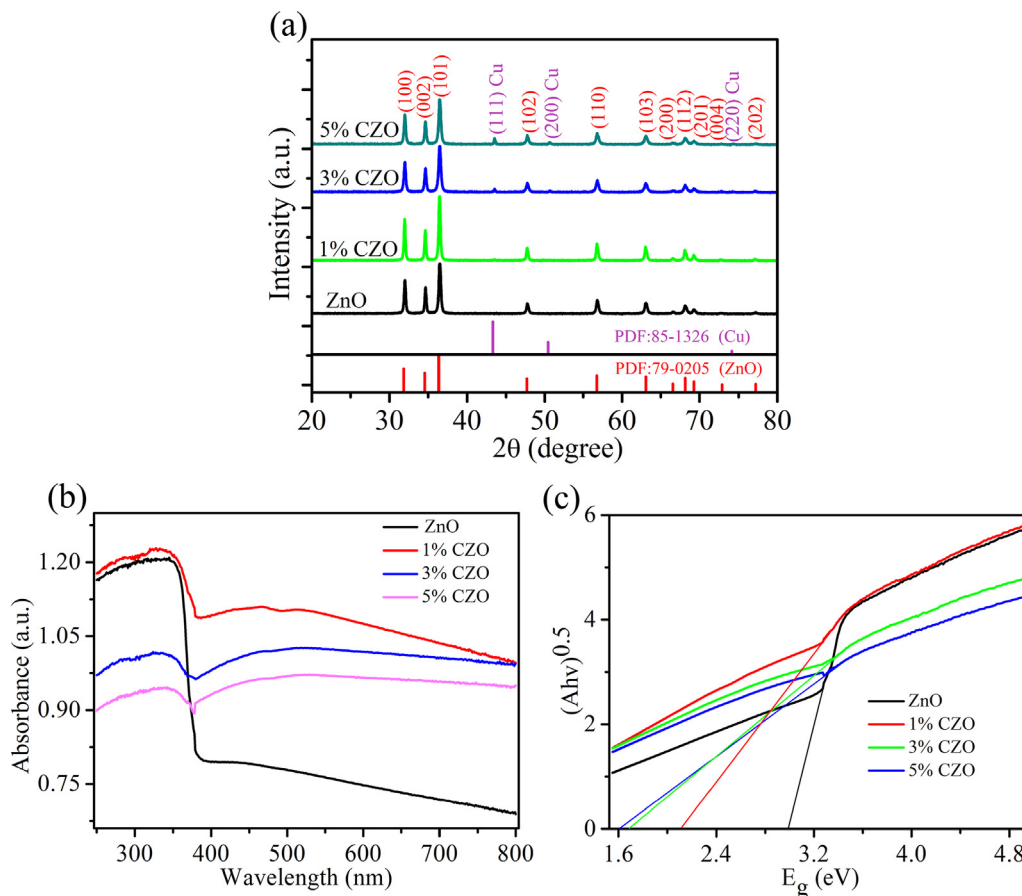


Fig. 1. (a) XRD, (b) UV-vis spectra and (c) band gap energies of ZnO and CZO.

all CZO samples correspond to (111), (200) and (220) faces of Cu (JCPDS No. 85-1326). In addition, all the diffraction peaks of ZnO and CZO are consistent, indicating Cu only modifies the surface of ZnO instead of being doped into the lattice of ZnO.

Fig. 1(b) shows the UV-vis absorption spectra of ZnO and CZO, where all samples show an absorption peak near 350 nm related to the exciton absorption of ZnO [21]. It is distinctly observed that the CZO exhibits an additional absorption band at 500–600 nm, which is related to surface plasmon resonance of Cu metal nanoparticles [39]. The optical band gap energies of ZnO, CZO (1 mol%), CZO (3 mol%) and CZO (5 mol%) are estimated by the Tauc's plots as in Fig. 1(c), and the corresponding values are 3.04 eV, 2.13 eV, 1.70 eV and 1.62 eV, respectively. The smaller bandgap of CZO indicates the fact that electrons can be more easily excited from valence band to conduction band and hence there are more photo-generated carriers which will reduce the resistance value.

Fig. 2 shows the scanning electron microscopy (SEM) and transmission electron microscopy (TEM) of ZnO, CZO (1 mol%), CZO (3 mol%) and CZO (5 mol%). In Fig. 2(a), pure ZnO shows there are irregular particles with a diameter of 0.08–1.2 μm. In Fig. 2(b), the morphology of CZO (1 mol%) nanoparticles becomes regular and the diameter ranges from 0.06 μm to 0.5 μm. In Fig. 2(c), ZnO particles aggregate into microspheres with a diameter of 2.2–3.4 μm. Moreover, the CZO microspheres are composed of small particles with a diameter from 40 nm to 70 nm. Such a structure makes the surface roughness and specific surface area increased. The particle size is small and uniform, which is conducive to the reaction between the CZO sensor and the target molecule. In Fig. 3(d), CZO (5 mol%) microspheres are stacked up and some were broken. The size of CZO (5 mol%) are from 1.08 μm to 2.2 μm. These results show that Cu modification precipitates gigantic changes structure of ZnO.

Fig. 2(e–h) shows the HRTEM images of ZnO, CZO (1 mol%), CZO (3 mol%) and CZO (5 mol%), respectively. As shown in Fig. 2(e), the average value of lattice spacing for (101) of ZnO planes is 0.247 nm [40]. In Fig. 2(f), the average values of lattice spacing for (100) of ZnO planes [41] and Cu (111) are 0.281 nm and 0.209 nm [42], respectively. In Fig. 2(g–h), the average values of lattice spacing for (101), (100) of ZnO planes and Cu (111) planes are 0.247 nm, 0.281 nm and 0.209 nm, respectively. These results are consistent with XRD results and indicate that CZO samples were successfully prepared.

The XPS spectra of Cu 2p, Zn 2p, O1s of ZnO, CZO (1 mol%), CZO (3 mol%) and CZO (5 mol%) are shown in Fig. 3. In Fig. 3(a), the binding energies of two characteristic peaks are observed at 932.18 and 951.98 eV, which are due to $2P_{3/2}$ and $2P_{1/2}$ states of Cu, respectively. The difference between the above two binding energies is 19.80 eV, indicating that the chemical valence of Cu is in the 0 valence state [43]. Fig. 3(b) shows that Zn $2P_{3/2}$ and Zn $2P_{1/2}$ peaks of ZnO are located at 1020.78 eV and 1043.86 eV, respectively. The difference between the two Zn 2p core levels is 23.08 eV, which indicates that the Zn atoms are in a +2 oxidation state [44]. In addition, the peak of Zn 2p in CZO sample shifts slightly towards larger binding energy compared with ZnO. This shift can be ascribed to the electron transfer between Zn^{2+} and Cu particles, which means the shielding effect from the most stable state of main Zn^{2+} to the unfilled electrons for Cu with higher charge density [45].

In Fig. 3(c–f), O 1s transition is decomposed into three peaks, where O_1 represents oxygen in ZnO crystal, O_2 represents oxygen vacancy or oxygen defect of the crystal, and O_3 represents oxygen free radicals ($O^{\bullet-}$: O_{ads}^- , O_{ads}^{2-} , O_{2ads}^-) on the surface of ZnO. The increase of O_2 can provide more active sites for sensing materials, which is conducive to gas adsorption [46]. The increase of O_3 will cause the redox reaction of the gas with more oxygen free radicals [5–6,8,10]. The contents of

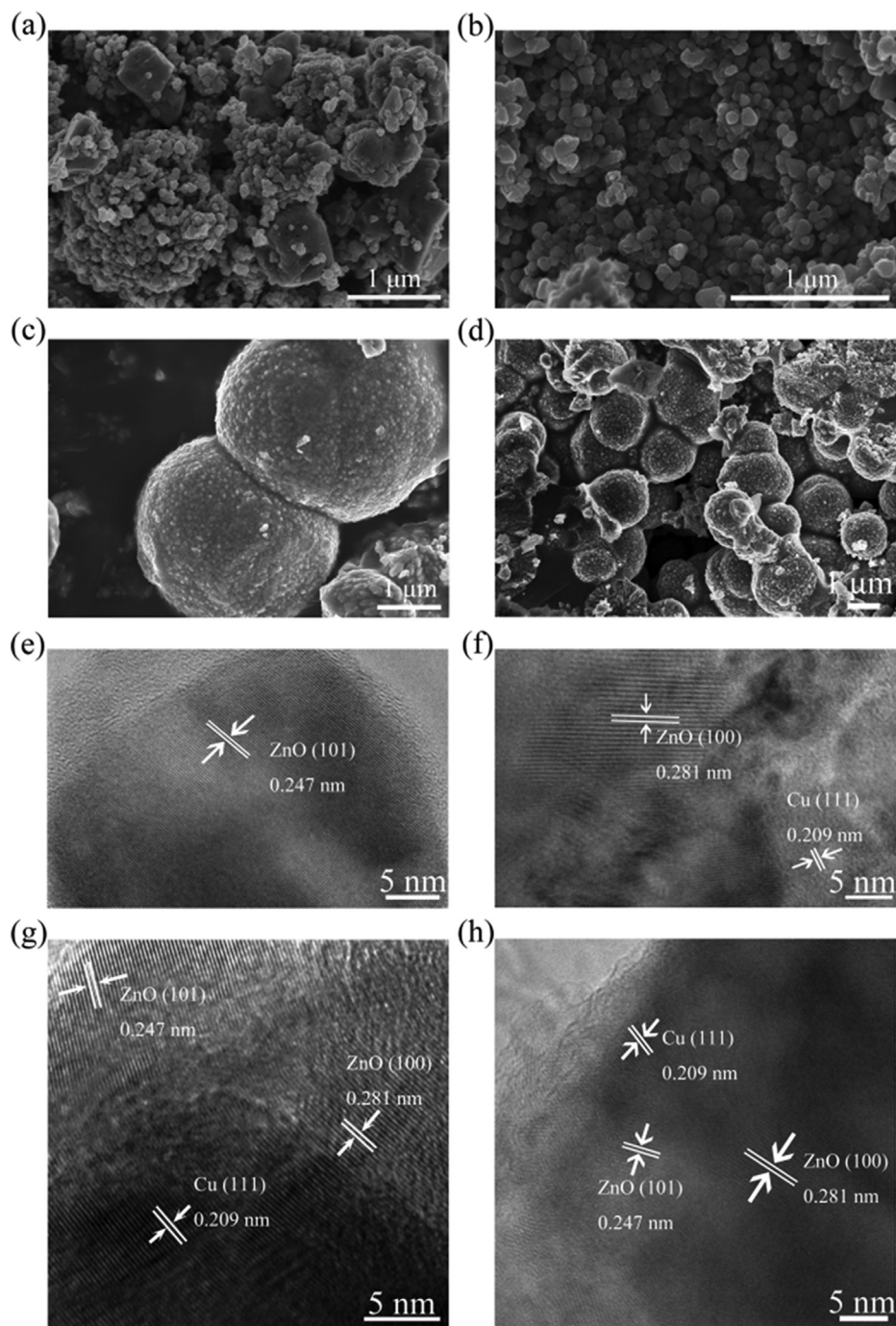


Fig. 2. SEM images of (a) ZnO, (b) CZO (1 mol%), (c) CZO (3 mol%) and (d) CZO (5 mol%). TEM images of (e) ZnO, (f) CZO (1 mol%), (g) CZO (3 mol%) and (h) CZO (5 mol%) with high resolution, respectively.

oxygen vacancies for ZnO, CZO (1 mol%), CZO (3 mol%) and CZO (5 mol%) are 27.50%, 20.99%, 19.58% and 27.35%, respectively. The contents of free oxygen on the surface of ZnO, CZO (1 mol%), CZO (3 mol%) and CZO (5 mol%) are 19.10%, 25.97%, 27.37% and 24.14%, respectively. As shows in XPS, CZO (3 mol%) has the most surface oxygen radicals O^* (O_{ads}^- , O_{ads}^{2-} , $O_{2\text{ads}}^-$). It is worth noting that CZO (3 mol%) has the smallest oxygen vacancy and the most surface oxygen free radicals.

Fig. 4 shows the FTIR spectra of ZnO, CZO (1 mol%), CZO (3 mol%) and CZO (5 mol%). The absorption peaks at 437.82, 455.03, 461.06 and 467.25 cm^{-1} are related to the bending vibration region of Zn-O bond [47]. The absorption peaks of 3309.86, 3496.40 and 3668.29 cm^{-1} are assigned to the hydroxyl group (O-H) stretching vibration modes due to

the expansion vibration of O-H base being appeared in the range of 3200–3670 cm^{-1} [48]. The amount of hydroxyl group decreases and then increases with Cu content increasing. It is worth noting that hydroxyl group disappears in CZO (3 mol%), which is due to the fact that two hydroxyls in the CZO sample are converted to water molecule and are removed during calcination.

3.2. Calculations of Cu-modified ZnO

To further investigate the mechanism of the disappearing of hydroxyl ($-OH$) in CZO (3 mol%), a possible reduction path of hydroxyl in CZO is presented in Fig. 5. Fig. 5(a) shows reactants in the reduction path of hydroxyl group. A Cu atom is located near a hydroxyl group and

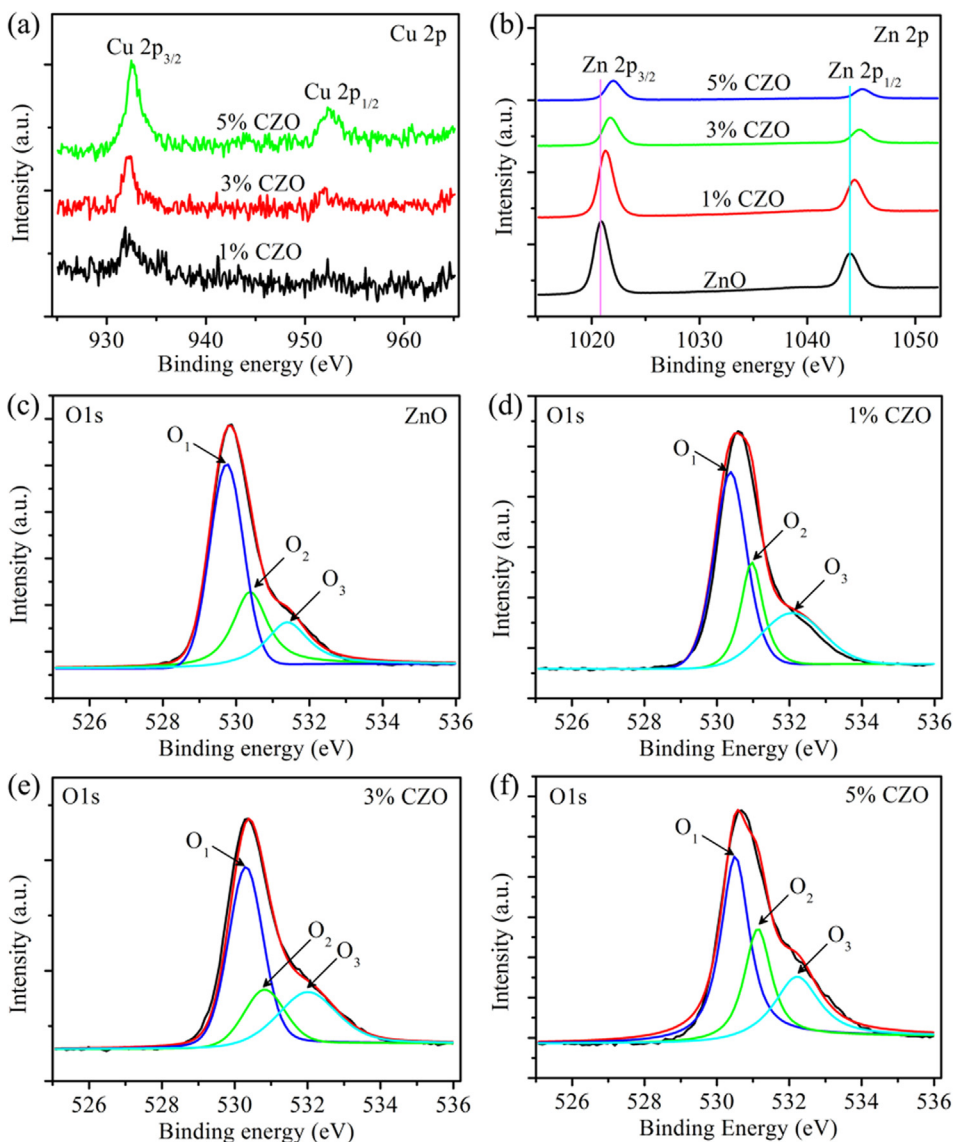


Fig. 3. XPS spectra of ZnO and CZO. (a) Cu 2p, (b) Zn 2p and (c–f) O 1s for ZnO, CZO (1 mol%), CZO (3 mol%) and CZO (5 mol%), respectively.

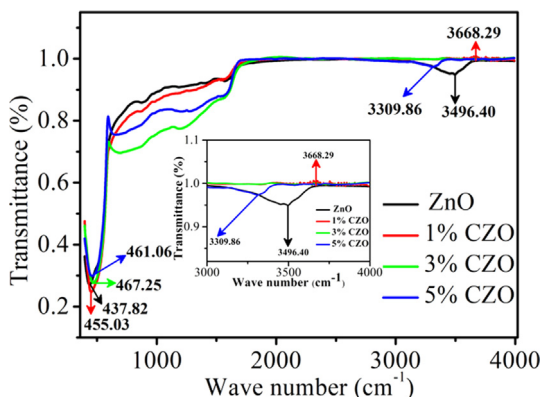


Fig. 4. FTIR spectra of ZnO, CZO (1 mol%), CZO (3 mol%) and CZO (5 mol%). The inset is the amplified image in a range of 3000–4000 cm^{-1} .

bound to two Zn atoms. The hydroxyl is bound to three Zn atoms on ZnO surface. The distance between Cu and oxygen atom in hydroxyl group is 3.60 Å. Fig. 5(b) shows the transition state corresponding to the energy barrier of 0.73 eV. The hydroxyl is bound to one Zn atom on

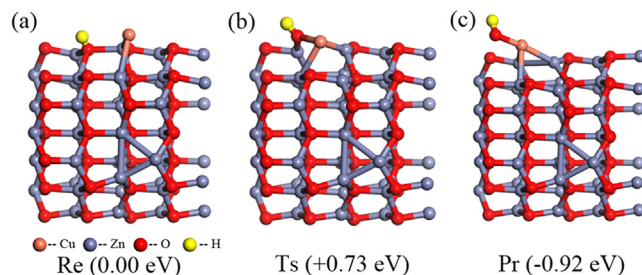


Fig. 5. Theoretical model of hydroxyl reduction path of Cu-modified ZnO composites. Pink, blue and red balls correspond to Cu, Zn and O atoms, respectively. (a) Reactant (Re), (b) transition state (Tr) and (c) product (Pr).

the surface. The distance between Cu and oxygen in hydroxyl is decreased from 3.60 Å to 2.21 Å, which means Cu atom shows a tendency to reduce hydroxyl and form an oxygen vacancy on the surface of ZnO. Fig. 5(c) shows the final product in the reduction path of hydroxyl. Compared with the transition state, Fig. 5(c) shows that hydroxyl is only bound to Cu atom to form an oxygen vacancy, and Cu is located on the site of oxygen vacancy. The whole reaction is an exothermic reaction of 0.92 eV. Although the hydroxyl group is bound to Cu atom on

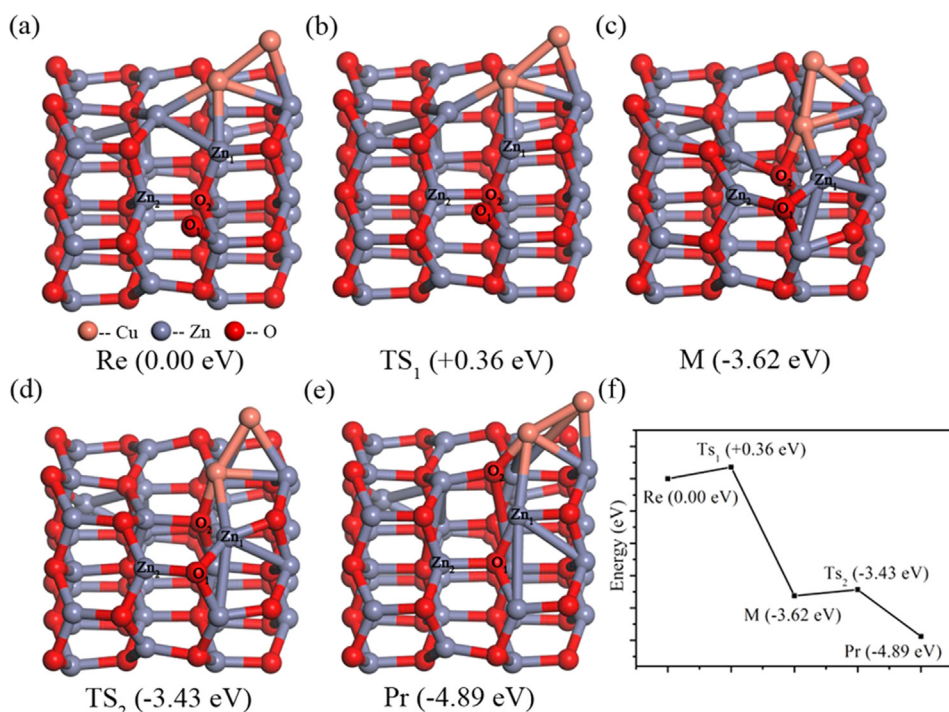


Fig. 6. Theoretical model for the occupied path by oxygen-vacancy in CZO. Cu, Zn and O atoms are colored with pink, blue and red, respectively. (a) Reactant (Re), (b) First transition state (TS₁), (c) Intermediate state (M), (d) Second transition state (TS₂), (e) Final product diagram (Pr), (f) Optimum energy occupied path of oxygen-vacancy.

the surface of ZnO, it can be removed by calcination at 600 °C. That means that the hydroxyl can be removed by two steps. Firstly, the hydroxyl group binds to Cu atoms, resulting in the reduction of the hydroxyl group on the surface of ZnO. Secondly, two hydroxyls form a water molecule and leave an oxygen atom on the surface of ZnO by calcination at 600 °C. Two hydroxyl calcination reaction is as the follow:



where star (*) denotes adsorption on the surface of the material. The resulted water molecules could be removed under calcination, and residual oxygen atoms are adsorbed on surface of ZnO. Fig. 5 could explain that the oxygen-vacancy is occupied by Cu atom and that leads to oxygen vacancy decrease (XPS). Furthermore it is also clarified the disappearance of O-H stretching vibration in Fig. 4.

Fig. 6 describes a theoretical model of the occupied path of oxygen-vacancy in CZO composite with no change for the basic model but only the selected part. Fig. 6(a) shows the reactant in the occupied path of an oxygen vacancy. Oxygen atom (O₁) in Fig. 6(a) corresponds to the residual oxygen atom in Fig. 5, and two Cu atoms are located on one oxygen vacancy. Fig. 6(b) shows that the reactant overcomes the barrier of 0.36 eV to form the first transition state (TS₁) in the path. The distance between O₁ and Zn₁ is reduced from 3.73 to 3.25 Å. Fig. 6(c) shows the intermediate state (M) in the path which can be formed from the first transition state by overcoming the barrier of 3.92 eV. In Fig. 6(c), O₁ is bound to two Zn atoms (Zn₁ and Zn₂) and Cu atom is bound to the oxygen atom (O₂). Compared with the TS₁, O₂ binds to one Cu atom and the bond between O₂-Zn₁ and O₂-Zn₂ are broken, hence there is a trend of O₂ moving to inside of ZnO as in Fig. 6(c). In addition, the coordination number of O₂ is decreased from 4 to 3 in this process, which makes O₂ easier to move towards to the interior of ZnO. Fig. 6(d) shows the second transition state (TS₂) in the path which is obtained from the intermediate state by overcoming a barrier of 0.19 eV. As shown in Fig. 6(d) for TS₂, O₂ is below the Cu atom. Fig. 6(e) shows the final product state (Pr) obtained by TS₂ overcoming a 1.46 eV barrier. In Fig. 6(e), O₂ atom occupies the oxygen-vacancy and O₁ replaces the position of O₂. It is clear that these residual oxygen atoms can force the internal oxygen atom of ZnO to occupy the oxygen

vacancy under the assistance of Cu atoms, and that should decrease the concentration of oxygen vacancies, which is consistent with the results in Fig. 3. Fig. 6(f) shows optimum energy occupied path for an oxygen vacancy in CZO composite corresponding to the energy as in Fig. 6(a–e). Fig. 6 illustrates that the Cu metal can split the oxygen molecules in the air to form a large number of free oxygen on the surface of ZnO, decreasing the current of CZO sensor, which is consistent with the highest O₃ content in Fig. 3. Furthermore, the oxygen radicals on the surface of the CZO react with HCHO molecules to form water and carbon dioxide when CZO is exposed to HCHO gas, increasing the current of the sensor. As a result, a large number of surface oxygen free radicals can oxidize and decompose more HCHO molecules, which means that Cu metal can improve the sensitivity of ZnO for HCHO detection.

Fig. 7(a) and (b) show the CZO structure and the structure of HCHO adsorption in CZO (3% mol). Fig. 7(c–d) shows the energy band structure of Fig. 7(a–b). We can clearly see that the band gap is reduced from 1.450 eV to 0.714 eV when HCHO molecule is adsorbed on Cu, which is due to that the HCHO molecule provides a local state. The low band gap increases the transition probability of electrons and makes it easier for electrons to transition from valence band to conduction band, which can accelerate the redox reaction on the surface of CZO.

Table 1 shows the band gap of CZO (3% mol) and different gas adsorption in CZO (3% mol) based on DFT calculation, where plus sign (+) means adsorption. The lowest band gap (0.714 eV) is obtained when HCHO is adsorbed in CZO (3% mol) sensor (3% CZO + HCHO) compared to other gases, which means CZO has better selectivity in the detection for HCHO.

3.3. Sensor testing and mechanism

Fig. 8 shows the dynamic response curves of HCHO, C₂H₆O, NH₃ and C₃H₆O vapors with a concentration of 5000 ppm for ZnO, CZO (1 mol%), CZO (3 mol%) and CZO (5 mol%) sensors at room temperature, where there are three consecutive cycles tested for each case. The response of the sensor herein is defined as response = ΔI/I_r = (I_r - I_g)/I_r, where I_r is the current in the reference gas (air) and I_g is the current in the target gas. The electric current increases when the sensor

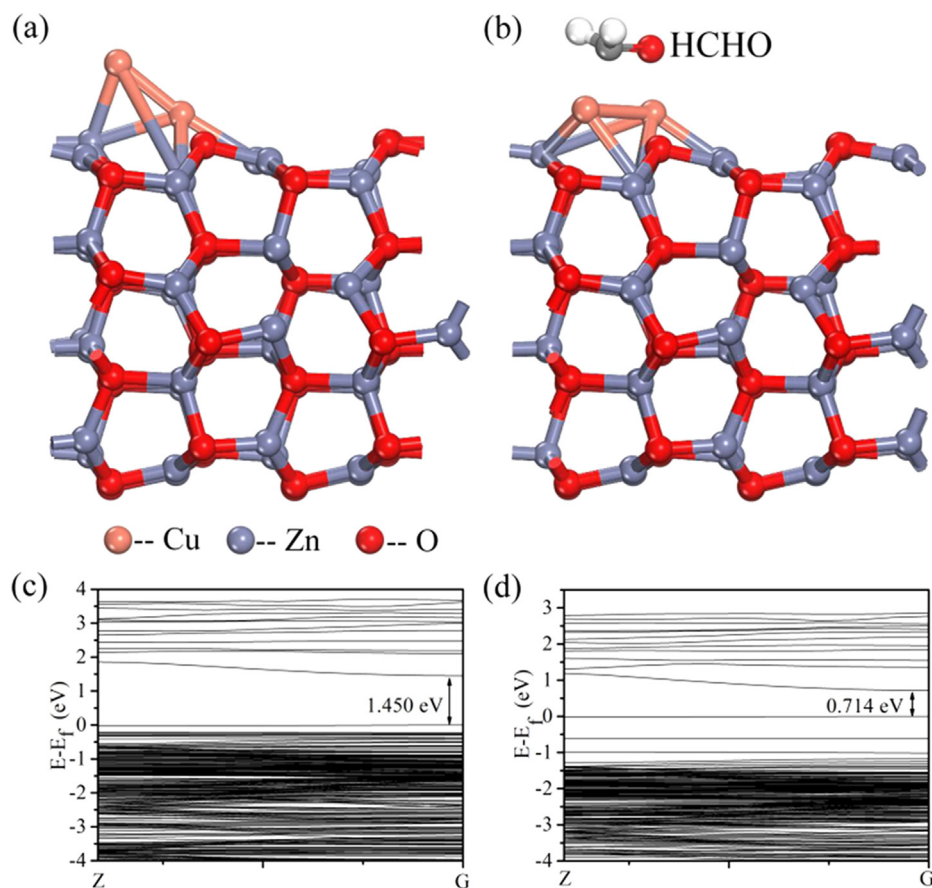


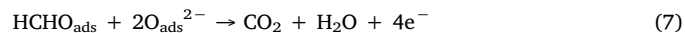
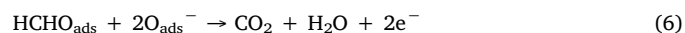
Fig. 7. Theoretical model of (a) CZO (3% mol) and (b) HCHO adsorption occurs in CZO (3% mol) (3% CZO + HCHO). (c) Energy band of CZO (3% mol) and (d) Energy band of 3% CZO + HCHO.

is immersed into HCHO, C₂H₆O, NH₃ and C₃H₆O vapor, while the electric current drops rapidly to its original value when the sensor is immersed into the air. The upward response curve reflects the characteristics of an n-type semiconductor [49]. Among these target gases, CZO sensors offer the best response to HCHO. Furthermore, the maximum responses of the CZO (3 mol%) for detecting HCHO in three consecutive cycles are all around 1300. The response of HCHO vapor reaches 0.13, 137.46, 1305.01 and 14.89 for ZnO and CZO (1 mol%), CZO (3 mol%) and CZO (5 mol%), respectively, which indicates that the addition of Cu metal can improve the response of ZnO sensor. The highest response of CZO (3 mol%) to HCHO vapor indicates that CZO (3 mol%) sensor has the best sensitivity to HCHO vapor.

In order to evaluate the effect of relative humidity (RH) on the performance of gas sensors at room temperature, the humidity test was performed using the CZO (3 mol%) gas sensor and 11% RH at room temperature (RT) as a base humidity [37]. The response was defined by $\text{response} = \Delta I/I_a = (I_b - I_a)/I_a$, where I_a is the current in the reference 11% RH and I_b is the current in the target humidity. As shown in Fig. 9, the response of CZO (3 mol%) corresponds to RH in the range from 11% to 75%, 11% to 85% and 11% to 95% RH are 0.42, 0.62 and 0.69, respectively. Small response indicates the excellent endurance to humidity conditions.

The sensing mechanism of CZO can be ascribed as two parts. Firstly, some oxygen molecules capture free electrons from the conduction

band to generate oxygen free radicals (O_{ads}^- , O_{ads}^{2-} , $O_{2\text{ads}}^-$) when oxygen molecules are adsorbed on the surface of CZO sensor in the air. The other oxygen molecules are split into two oxygen atoms by Cu which is easier to capture free electrons to produce oxygen free radicals (O_{ads}^- and O_{ads}^{2-}) compared with oxygen molecules. Secondly, HCHO molecules will be adsorbed on the Cu metal when CZO sensor is in the HCHO vapors, thus reducing the band gap of CZO. Then HCHO molecules are adsorbed on the Cu metal (HCHO_{ads}) to react with the adsorbed oxygen ions O^* (O^* : O_{ads}^- , O_{ads}^{2-} , $O_{2\text{ads}}^-$) to form CO₂ and H₂O. The electrical resistance is decreased and the current of CZO is increased due to the releasing of electrons. The reaction processes are as follows:



Statistical analyses of response for different target gases is useful to better understand the overall performance of the CZO sensor as shown Fig. 10(a). As can be seen from Fig. 10(a), the CZO (3 mol%) sensor has the highest response to HCHO vapor and the response is increased from 0.13 to 1300, indicating that the addition of Cu metal improves the

Table 1
Band gap of CZO (3% mol) and different gas adsorption in CZO (3% mol).

	3% CZO	3% CZO + HCHO	3% CZO + NH ₃	3% CZO + C ₂ H ₆ O	3% CZO + C ₃ H ₆ O
Band gap (eV)	1.450	0.714	0.987	1.304	1.297

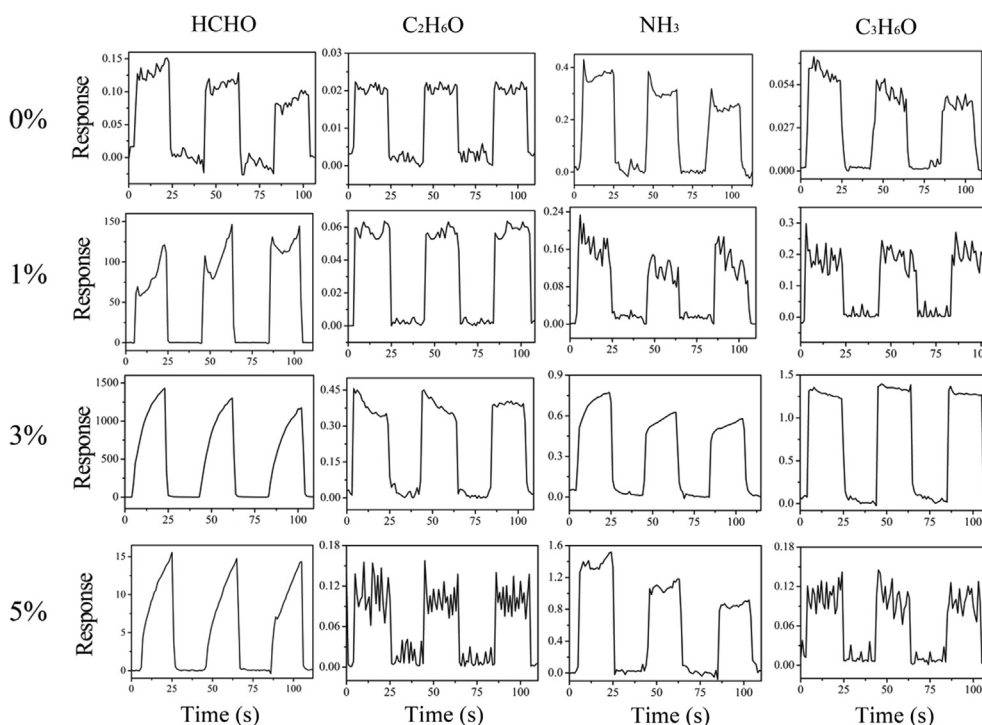


Fig. 8. Dynamic sensing curves of HCHO, C₂H₆O, NH₃ and C₃H₆O vapors with a concentration of 5000 ppm using ZnO and CZO (1 mol%), CZO (3 mol%) and CZO (5 mol%) based sensors at room temperature.

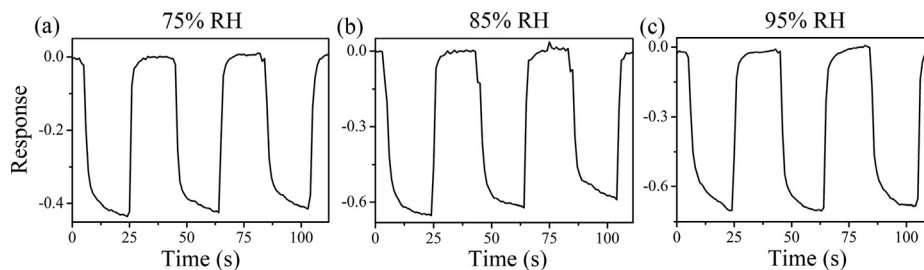


Fig. 9. Response curves of the CZO (3 mol%) sensor to 75%, 85% and 95% RH at room temperature.

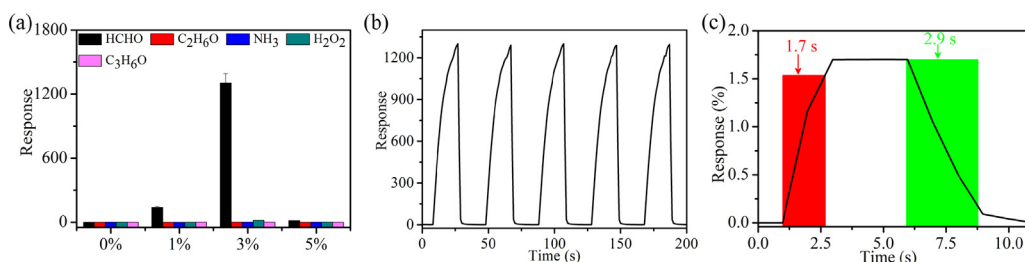


Fig. 10. (a) Histogram response plot of average maximum response for three consecutive cycles of HCHO, C₂H₆O, NH₃, H₂O₂ and C₃H₆O vapors with a concentration of 5000 ppm at room temperature. (b) Cyclic transient response curve of CZO (3 mol%) to 5000 ppm HCHO. (c) Response and recovery time curve of CZO (3 mol%) to 1 ppm HCHO.

Table 2

Comparison of the performance between our HCHO sensor based on CZO (3 mol%) and reported HCHO sensors based on other semiconductors.

Materials	Temperature (°C)	limit of detection (ppm)	Response/Recovery time	Concentration (ppm)	References
Au@SnO ₂	25 °C	20	80 s/62 s	50	[51]
ZnO/Graphene nanocomposites	25 °C	25	30 s/40 s	100	[52]
Pt-decorated MoO ₃ nanowires	25 °C	1	17.8 s/10.5 s	100	[53]
Pt-decorated MoO ₃ nanowires	25 °C	1	8.8 s/0.94 s	1	[53]
ZnO nanoplates	25 °C(UV light)	5	97 s/86 s	100	[54]
ZnO nanoflowers	25 °C(UV light)	5	44 s/104 s	100	[54]
PEI/TiO ₂ nanoporous fibers	25 °C	1	120 s/–	1	[55]
ZnO/rGO	25 °C	2	45.8 s/–	2	[56]
Cu-modified ZnO	25 °C	0.61	1.7 s/2.9 s	1	This work

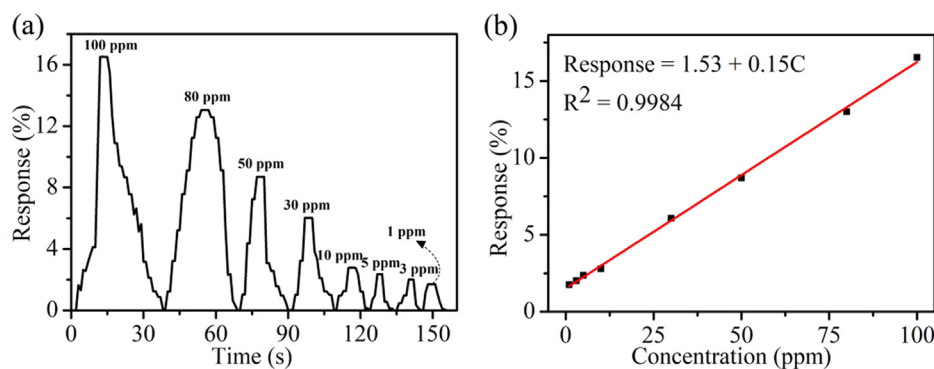


Fig. 11. Linearity of the response of the CZO (3 mol%) sensor to HCHO. (a) Response curves with concentration varying from 1 to 100 ppm at room temperature. (b) Corresponding fitting curve of (a).

response of ZnO sensor. The binding energies of CZO (3 mol%) and pure ZnO for HCHO are calculated to be 0.75 eV and 0.54 eV by first-principles using Eq. (2) and the corresponding theoretical model can be shown in Fig. 7(b). It is worth noting that the highest response is related to the highest binding energy of CZO, which means that a higher binding energy allows more HCHO molecules to react with free oxygen on the surface of CZO. In order to verify the performance of the CZO (3 mol%) sensor, five cycle tests have been performed as shown in Fig. 10(b). Fig. 10(b) shows the cyclic transient response curve of 3% CZO to 5000 ppm HCHO. The maximum responses of the CZO (3 mol%) five consecutive cycles are all around 1300 and response/recovery behavior can be repeated easily. The recycle experiment shows that CZO (3 mol%) has good repeatability.

Generally, rapid response time and recovery time of sensors are beneficial for practical applications. Response time refers to the time required for the sensor's resistance to reach 90% value of the steady-state after the sensor is exposed to measured gas. Recovery time refers to the time taken for the measured gas to detach from the sensor surface until the resistance reduces to 90% value of the steady-state [50]. Fig. 10(c) shows the response time and recovery time of CZO (3 mol%) sensor for 1 ppm of HCHO vapor detection at room temperature. Here, red and green bars represent the response time and recovery time of 1.7 s and 2.9 s, respectively.

The sensing performance of our HCHO gas sensor based on CZO (3 mol%) and other semiconductor materials are listed in Table 2. Compared with the other HCHO sensors, the HCHO sensor based on CZO (3 mol%) in this experiment has the LOD of 0.61 ppm and a relatively fast response/recovery time (1.7 s/2.9 s) at a concentration of 1 ppm at room temperature. These results show that CZO gas sensor has high sensitivity and fast response to HCHO.

Fig. 11 depicts the linearity test for the response of the CZO (3 mol%) sensor to HCHO. Fig. 11(a) shows that the response-recovery time curve for HCHO vapor in the range from 1 to 100 ppm at room temperature. The real-time response of the sensor increases with the concentration of HCHO, and there is a linear relationship between the response and the concentration for HCHO as shown in plotted Fig. 11(b). The linear relationship between the response and HCHO vapor concentration (C) can be fitted in the range of 1–100 ppm from that response = $1.53 + 0.15C$ ($R^2 = 0.9984$). It indicates that low concentration gas can be quantitatively analyzed by the gas sensor designed in this experiment. The limit detection can be defined SD/m with m to be the slope of linear part of calibration curve and SD the standard deviation of the noise in response curve [50]. From Fig. 11(b), the limit detection of HCHO can be calculated to be 0.61 ppm.

4. Conclusion

HCHO gas sensors based on CZO were prepared by the sol-gel method and the sensing mechanism was studied by the first-principles

modeling. Experiments show that Cu metal can produce a large number of surface oxygen free radicals on the surface of ZnO and increase the binding energy of HCHO to CZO, which can effectively improve the performance of the HCHO sensor based on ZnO at room temperature. Furthermore, the CZO gas sensor exhibits excellent humidity resistance. Calculation shows that compared with other gases, the lowest band gap (0.714 eV) is acquired when HCHO adsorbed in CZO sensor, which means CZO has better selectivity in the detection of HCHO. Furthermore, Cu metal splits oxygen molecules in the air to form a large number of oxygen radicals on the surface of ZnO, which can oxidize and decompose more HCHO molecules. Compared with pure ZnO, CZO has a higher binding energy to HCHO due to Cu occupying oxygen vacancies leading to the disappearance of hydroxyl groups during calcination, which is more favorable to capture HCHO molecules and carry out redox reaction on the surface of ZnO. Such a highly sensitive, selective and stable gas sensor expands the application prospects in the field of HCHO detection.

CRediT authorship contribution statement

Yan Chen: Data curation, Investigation, Writing - original draft, Writing - review & editing. **Yong Zhang:** Supervision, Formal analysis. **Hongyan Zhang:** Conceptualization, Formal analysis, Funding acquisition, Supervision, Investigation, Methodology, Writing - review & editing. **Chu Chen:** Software, Supervision, Validation, Visualization.

Declaration of Competing Interest

The authors declare that they have no known competing financial interests or personal relationships that could have appeared to influence the work reported in this paper.

Acknowledgements

We thank the financial support from the National Natural Science Foundation of China (No.61665011, 11864039), National Science Foundation of Xinjiang Science and Technology Project (No. 2019D01C036) and the China Scholarship Council (No. 201808655040).

Appendix A. Supplementary material

Supplementary data to this article can be found online at <https://doi.org/10.1016/j.apsusc.2020.147446>.

References

- [1] K.M. Zhu, S.Y. Ma, Y. Tie, Q.X. Zhang, W.Q. Wang, S.T. Pei, X.L. Xu, Highly sensitive formaldehyde gas sensors based on Y-doped SnO₂ hierarchical flower-shaped

- nanostuctures, *J. Alloys. Compd.* 792 (2019) 938–944.
- [2] R. Zhang, S.Y. Ma, Q.X. Zhang, K.M. Zhu, Y. Tie, S.T. Pei, B.J. Wang, J.L. Zhang, Highly sensitive formaldehyde gas sensors based on Ag doped Zn₂SnO₄/SnO₂ hollow nanospheres, *Mater. Lett.* 254 (2019) 178–181.
- [3] O. Bunkoed, F. Davis, P. Kanatharana, P. Thavarungkul, S.P. Higson, Sol-gel based sensor for selective formaldehyde determination, *Anal. Chim. Acta.* 659 (2010) 251–257.
- [4] X.F. Wang, B. Ding, M. Sun, J.Y. Yu, G. Sun, Nanofibrous polyethyleneimine membranes as sensitive coatings for quartz crystal microbalance-based formaldehyde sensors, *Sensors Actuators, B Chem.* 144 (2010) 11–17.
- [5] Y.X. Li, N. Chen, D.Y. Deng, X.X. Xing, X.C. Xiao, Y.D. Wang, Formaldehyde detection: SnO₂ microspheres for formaldehyde gas sensor with high sensitivity, fast response/recovery and good selectivity, *Sensors Actuators, B Chem.* 238 (2017) 264–273.
- [6] Z.D. Wang, T. Zou, X.X. Xing, R.J. Zhao, Z.Z. Wang, Y. Yang, Y.D. Wang, CdIn₂O₄ nanoporous thin film gas-sensor for formaldehyde detection, *Physica.* 103 (2018) 18–24.
- [7] X.J. Tang, Y. Bai, A. Duong, M.T. Smith, L.Y. Li, L.P. Zhang, Formaldehyde in China: Production, consumption, exposure levels, and health effects, *Environ Int.* 35 (2009) 1210–1224.
- [8] R. Xu, L.-X. Zhang, M.-W. Li, Y.-Y. Yin, J. Yin, M.-Y. Zhu, J.-J. Chen, Y. Wang, L.-J. Bie, Ultrathin SnO₂ nanosheets with dominant high-energy 001 facets for low temperature formaldehyde gas sensor, *Sensors Actuators, B Chem.* 289 (2019) 186–194.
- [9] J.P. Cheng, J. Wang, Q.Q. Li, H.G. Liu, Y. Li, A review of recent developments in tin dioxide composites for gas sensing application, *J. Ind. Eng. Chem.* 44 (2016) 1–22.
- [10] D. Wang, M.L. Zhang, Z.L. Chen, H.J. Li, A.Y. Chen, X.Y. Wang, J.H. Yang, Enhanced formaldehyde sensing properties of hollow SnO₂ nanofibers by graphene oxide, *Sensors Actuators, B Chem.* 250 (2017) 533–542.
- [11] J.F. Chao, Y.H. Chen, S.M. Xing, D.L. Zhang, W.L. Shen, Facile fabrication of ZnO/C nanoporous fibers and ZnO hollow spheres for high performance gas sensor, *Sensors Actuators, B Chem.* 298 (2019) 126927.
- [12] F.L. Meng, H.X. Zheng, Y.F. Sun, M.Q. Li, J.H. Liu, Trimethylamine sensors based on Au-modified hierarchical porous single-crystalline ZnO nanosheets, *Sensors-Basel.* 17 (2017) 1424–8220.
- [13] Y.B. Shen, W. Wang, X.X. Chen, B.Q. Zhang, D.Z. Wei, S.L. Gao, B.Y. Cui, Nitrogen dioxide sensing using tungsten oxide microspheres with hierarchical nanorod-assembled architectures by a complexing surfactant-mediated hydrothermal route, *J. Mater. Chem. A.* 4 (2016) 1345–1352.
- [14] W. Liu, Y.L. Xie, T.X. Chen, Q.X. Lu, S.U. Rehman, L. Zhu, Rationally designed mesoporous In₂O₃ nanofibers functionalized Pt catalysts for high-performance acetone gas sensors, *Sensors Actuators, B Chem.* 298 (2019) 126871.
- [15] Z.H. Wang, R.X. Zhang, F.B. Gu, D.M. Han, Facile synthesis of facile synthesis of In₂O₃ nanoparticles with high response to formaldehyde at low temperature, *Int. J. Appl. Ceram. Tec.* 16 (2019) 1570–1580.
- [16] V. Kruefu, U. Inpan, P. Leangtanom, C. Arkarvipath, P. Kongpark, D. Phokharatkul, A. Wisitsoraat, A. Tuantranont, S. Phanichphant, Enhanced Gas-Sensing performances of Ru-loaded p-type Co₃O₄ nanoparticles, *Phys. Status. Solidi. A.* 215 (2018) 1701015.
- [17] D. Meng, D.Y. Liu, G.S. Wang, Y.B. Shen, X.G. San, M. Li, F.L. Meng, Low-temperature formaldehyde gas sensors based on NiO-SnO₂ heterojunction microflowers assembled by thin porous nanosheets, *Sensors Actuators, B Chem.* 273 (2018) 418–428.
- [18] M.H. Cao, Y.D. Wang, T. Chen, M. Antonietti, M. Niederberger, A highly sensitive and fast-responding ethanol sensor based on CdIn₂O₄ nanocrystals synthesized by a nonaqueous sol-gel route, *Chem. Mater.* 20 (2008) 5781–5786.
- [19] S.S. Shinde, P.S. Shinde, Y.W. Oh, D. Haranath, C.H. Bhosale, K.Y. Rajpure, Structural, optoelectronic, luminescence and thermal properties of Ga-doped zinc oxide thin films, *Appl. Surf. Sci.* 258 (2012) 9969–9976.
- [20] G. Murugadoss, Synthesis and characterization of transition metals doped ZnO nanorods, *J. Mater. Sci. Technol.* 28 (2012) 587–593.
- [21] S.G. Yu, H.Y. Zhang, C. Chen, C.C. Lin, Investigation of humidity sensor based on Au modified ZnO nanosheets via hydrothermal method and first principle, *Sensors Actuators, B Chem.* 287 (2019) 526–534.
- [22] Q.Q. Jia, H.M. Ji, Y. Zhang, Y.L. Chen, X.H. Sun, Z.G. Jin, Rapid and selective detection of acetone using hierarchical ZnO gassensor for hazardous odor markers application, *J. Hazard. Mater.* 276 (2014) 262–270.
- [23] M. Das, D. Sarkar, One-pot synthesis of zinc oxide-polyaniline nanocomposite for fabrication of efficient room temperature ammonia gas sensor, *Ceram. Int.* 43 (2017) 11123–11131.
- [24] D.L. Zhang, J.B. Zhang, Z. Guo, X.S. Miao, Optical and electrical properties of zinc oxide thin films with low resistivity via Li-N dual-acceptor doping, *J. Alloy. and Compd.* 509 (2011) 5962–5968.
- [25] J.-H. Kim, J.-H. Lee, Y.J. Park, J.-Y. Kim, A. Mirzaei, H.W. Kim, S.S. Kim, Toluene- and benzene-selective gas sensors based on Pt- and Pd-functionalized ZnO nanowires in self-heating mode, *Sensors Actuators, B Chem.* 294 (2019) 78–88.
- [26] O. Lupan, V. Postica, N. Wolff, J. Su, F. Labat, I. Ciofini, H. Cavers, R. Adelung, O. Polonsky, F. Faupel, L. Kienle, B. Viana, T. Pauporté, Low-temperature solution synthesis of Au-modified ZnO Nanowires for highly efficient hydrogen nanosensors, *ACS Appl. Mater. Interfaces.* 11 (2019) 32115–32126.
- [27] Y. Wang, X.N. Meng, M.X. Yao, G. Sun, Z.Y. Zhang, Enhanced CH₄ sensing properties of Pd modified ZnO nanosheets, *Ceram. Int.* 45 (2019) 13150–13157.
- [28] I.A. Pronin, D.T. Dimitrov, L.K. Krasteva, K.I. Papazova, I.A. Averin, A.S. Chanachev, A.S. Bojinova, A.T. Georgieva, N.D. Yakushova, V.A. Moshnikov, Theoretical and experimental investigations of ethanol vapour sensitive properties of junctions composed from produced by sol-gel technology pure and Fe modified nanostructured ZnO thin films, *Sensors Actuators, A Phys.* 206 (2014) 88–96.
- [29] R.S. Ganesh, E. Durgadevi, M. Navaneethan, V.L. Patil, S. Ponnusamy, C. Muthamizhchelvan, S. Kawasaki, P.S. Patil, Y. Hayakawa, Tuning the selectivity of NH₃ gas sensing response using Cu-doped ZnO nanostructures, *Sensors Actuators, A Phys.* 269 (2018) 331–341.
- [30] C.C. Lin, H.Y. Zhang, J. Zhang, C. Chen, Enhancement of the humidity sensing performance in Mg-doped hexagonal ZnO microspheres at room temperature, *Sensors.* 19 (3) (2019) 519.
- [31] R. Peña-García, Y. Guerra, B.V.M. Farias, D. Martínez Buitrago, A. Franco Jr, E. Padrón-Hernández, Effects of temperature and atomic disorder on the magnetic phase transitions in ZnO nanoparticles obtained by sol gel method, *Mater. Lett.* 233 (2018) 146–148.
- [32] Y. Zhang, K.F. Bai, Z.Y. Fu, C.L. Zhang, H. Zhou, L.G. Wang, S.J. Zhu, S.K. Guan, D.S. Li, J.H. Hu, Composite coating prepared by micro-arc oxidation followed by sol-gel process and in vitro degradation properties, *Appl. Surf. Sci.* 258 (2012) 2939–2943.
- [33] J.P. Perdew, A. Zunger, Self-interaction correction to density-functional approximations for many-electron systems, *Phys. Rev. B.* 23 (1981) 5048–5079.
- [34] K.P. Yuan, X.L. Zhang, D.W. Tang, M. Hu, Anomalous pressure effect on the thermal conductivity of ZnO, GaN, and AlN from first-principles calculations, *Phys. Rev. B.* 98 (2018) 144303.
- [35] J.N. Ma, W. Zhang, J.Y. Lin, Y. Sun, J.G. Ma, H.Y. Xu, Y.C. Liu, G.C. Yang, Theoretical study on group III elements and F co-doped ZnO, *J. Alloy. Compd.* 819 (2020) 153012.
- [36] N. Govind, M. Petersen, G. Fitzgerald, D. King-Smith, J. Andzelm, A generalized synchronous transit method for transition state location, *Comp. Mater. Sci.* 28 (2003) 250–258.
- [37] C. Chen, W.X. Kong, H.-M. Duan, J. Zhang, Theoretical simulation of reduction mechanism of graphene oxide in sodium hydroxide solution, *Phys. Chem. Chem. Phys.* 16 (2014) 12858–12864.
- [38] C. Chen, J. Zhang, B. Zhang, H.M. Duan, Hydrogen adsorption of Mg-doped graphene oxide: A first-principles study, *J. Phys. Chem. C* 117 (2013) 4337–4344.
- [39] J.L. Duan, T.W. Cornelius, J. Liu, S. Karim, H.J. Yao, O. Picht, M. Rauber, S. Müller, R. Neumann, Surface plasmon resonances of Cu nanowire arrays, *J. Phys. Chem. C.* 113 (2019) 13583–13587.
- [40] W.N. Wang, L.H. Xu, R.F. Zhang, J.L. Xu, F.L. Xian, J. Su, F. Yang, Coexistence of ferromagnetism and paramagnetism in ZnO/CuO nanocomposites, *Chem. Phys. Lett.* 721 (2019) 57–61.
- [41] H.Y. Zhang, S.G. Yu, C. Chen, J. Zhang, J. Liu, P. Li, Effects on structure, surface oxygen defects and humidity performance of Au modified ZnO via hydrothermal method, *Appl. Surf. Sci.* 486 (2019) 482–489.
- [42] H.X. Li, X. Li, W. Dong, J.H. Xi, G. Du, Z.G. Ji, Cu nanoparticles hybridized with ZnO thin film for enhanced photoelectrochemical oxygen evolution, *J. Alloys. Compd.* 768 (2018) 830–837.
- [43] T.F. Long, H.M. He, J.Z. Li, M.K. Yuan, J.J. Wei, Z.D. Liu, Optically active Au – Cu bimetallic nanoclusters: Insights into the alloying effect on the chiroptical behavior, *J. Phys. Chem. C.* 122 (2018) 11152–11158.
- [44] S. Wu, Z.W. Chen, T. Wang, X.H. Ji, A facile approach for the fabrication of Au/ZnO-hollow-sphere-monolayer thin films and their photocatalytic properties, *Appl. Surf. Sci.* 412 (2017) 69–76.
- [45] G.L. Kabongo, G.H. Mhlongo, B.M. Mthudi, K.T. Hillie, P.S. Mbule, M.S. Dhlamini, Structural, photoluminescence and XPS properties of Tm³⁺ ions in ZnO nanostructures, *J. Lumim.* 187 (2017) 141–153.
- [46] C. Wang, X.B. Cui, J.Y. Liu, X. Zhou, X.Y. Cheng, P. Sun, X.L. Hu, X.W. Li, J. Zheng, G. Lu, Design of superior ethanol gas sensor based on Al-doped NiO nanorod-flowers, *ACS Sens.* 1 (2016) 131–136.
- [47] J.E. Rodriguez-Paez, A.C. Caballero, M. Villegas, C. Moure, P. Duran, J.F. Fernandez, Controlled precipitation methods: formation mechanism of ZnO nanoparticles, *J. Eur. Ceram. Soc.* 21 (2001) 925–930.
- [48] D. Scaranou, S. Bertarione, G. Spoto, A. Zecchina, C.O. Areal, FTIR spectroscopy of hydrogen, carbon monoxide, and methane adsorbed and co-adsorbed on zinc oxide, *Thin Solid Films* 400 (2001) 50–55.
- [49] Q.H. Sun, Z.F. Wu, H.M. Duan, D.Z. Jia, Detection of Triacetone Triperoxide (TATP) Precursors with an array of sensors based on MoS₂/RGO composites, *Sensors* 19 (2019) 1281.
- [50] L.N. Shao, Z.F. Wu, H.M. Duan, T. Shaymurat, Discriminative and rapid detection of ozone realized by sensor array of Zn²⁺ doping tailored MoS₂ ultrathin nanosheets, *Sensors Actuators, B Chem.* 259 (2018) 937–946.
- [51] F.C. Chung, R.-J. Wu, F.-C. Cheng, Fabrication of a Au@SnO₂ core-shell structure for gaseous formaldehyde sensing at room temperature, *Sensors Actuators, B Chem.* 190 (2014) 1–7.
- [52] Q.W. Huang, D.W. Zeng, H.Y. Li, C.S. Xie, Room temperature formaldehyde sensors with enhanced performance, fast response and recovery based on zinc oxide quantum dots/graphene nanocomposites, *Nanoscale.* 4 (2012) 5651–5658.
- [53] X.X. Fu, P.Y. Yang, X.F. Xiao, D. Zhou, R. Huang, X.H. Zhang, F. Cao, J. Xiong, Y.M. Hu, Y.F. Tu, Y.A. Zou, Z. Wang, H.S. Gu, Ultra-fast and highly selective room-temperature formaldehyde gas sensing of Pt-decorated MoO₃ nanobelts, *J. Alloys. Compd.* 797 (2019) 666–675.
- [54] J.B. Cui, L.G. Shi, T.F. Xie, D.J. Wang, Y.H. Lin, UV-light illumination room temperature HCHO gas-sensing mechanism of ZnO with different nanostructures, *Sensors Actuators, B Chem.* 227 (2016) 220–226.
- [55] X.F. Wang, F.H. Cui, J.Y. Lin, B. Ding, J.Y. Yu, S.S. Al-Deyab, Functionalized nanoporous TiO₂ fibers on quartz crystal microbalance platform for formaldehyde sensor, *Sensors Actuators, B Chem.* 171–172 (2012) 658–665.
- [56] X. Li, J. Wang, D. Xie, J.L. Xua, R.X. Daia, L. Xiang, H.W. Zhu, Y.D. Jiang, Reduced graphene oxide/hierarchical flower-like zinc oxide hybrid films for room temperature formaldehyde detection, *Sensors Actuators, B Chem.* 221 (2015) 1290–1298.